Current Research in Neurobiology 3 (2022) 100045

Contents lists available at ScienceDirect

Current Research in Neurobiology

journal homepage: www.sciencedirect.com/journal/current-research-in-neurobiology

Microstructural interactions contribute to the hotspot in the living cochlea

Junpei Liu [a,c,1], Yanru Bai [a,c,1], Qianli Cheng [b], Shu Zheng [a,c], Stephen Elliott [d,**], Guangjian Ni [a,b,c,*]

[a] Academy of Medical Engineering and Translational Medicine, Tianjin University, Tianjin, 300072, China
[b] Department of Biomedical Engineering, College of Precision Instruments and Optoelectronics Engineering, Tianjin University, Tianjin, 300072, China
[c] Tianjin Key Laboratory of Brain Science and Neuroengineering, Tianjin, 300072, China
[d] Institute of Sound and Vibration Research, University of Southampton, Southampton, SO17 1BJ, UK

ARTICLE INFO

Keywords:
Hotspot
Organ of Corti
Finite element model
Low-frequency

ABSTRACT

The mechanism of the active cochlea relies on a complex interaction between microstructures in the organ of Corti. A significant longitudinal vibration "hotspot" was recently observed in the high-frequency region of the living gerbil cochlea between the Deiters cells and the outer hair cells. A similar phenomenon was also found in guinea pigs with a relatively smaller magnitude. The cause is unknown, but one hypothesis is that this phenomenon is due to the structural constraints between different microstructures. It is not easy to explain the mechanism of hotspots directly from experimental observations. It may also be difficult to image or test if the hotspot will occur in the low-frequency region in the cochlea. We built two three-dimensional finite element models corresponding to the high- and low-frequency regions in the guinea pig cochlea. Responses of the organ of Corti to passive acoustic and outer hair cell electrical excitation were calculated. The two excitations were then superimposed to predict the active response of the organ of Corti. The hotspot phenomenon in the experiment was reproduced and analyzed in-depth about influencing factors. Our results indicate that hotspots appear in the low-frequency region of the cochlea as well. We hypothesize that the hotspot is a locally originated phenomenon in the cochlea, and the traveling wave further enhances the response to low-frequency excitation. The movement of outer hair cells inclined in the longitudinal direction is the leading cause of the hotspot.

1. Introduction

The active amplification mechanism of the cochlea is related to the microscopic movement in the organ of Corti (OC) (Robles and Ruggero, 2001; von Bekesy, 1970). At present, our understanding of this mechanism mainly relies on measurements in animal experiments. Attention has been paid to the transverse movement of the basilar membrane (BM), reticular lamina (RL), and tectorial membrane (TM), and differences in the amplitude and phase were found (He et al., 2018; Ren et al., 2016). Recent experiments have started to explore the areas of Deiters cells (DCs) and outer hair cells (OHCs) (Cooper et al., 2018). They found that in the high-frequency region of the living gerbil cochlea, the longitudinal response is significant and even greater than that of the basilar membrane. This response is most evident near the connection between OHCs and DCs, called "hotspot". Similarly, Fallah et al. (2021) found that hotspot responses also occur in the guinea pig, but the response magnitude was smaller than the gerbil. Cooper et al. (2018) proposed that this phenomenon is driven by the movement of OHCs, under the structural constraints of the organ of Corti. According to their hypothesis, a similar response may also occur in the low-frequency region of the cochlea, although this has not been observed experimentally yet.

This paper studied the hotspot using three-dimensional segmental finite element models of the cochlea. Such models could reproduce experimentally observed results and test different hypotheses. Our work showed that the hotspot could be simulated under the following conditions:

(1) Including a three-dimensional structure that can simulate longitudinal movement.
(2) Including the Phalangeal process (PhPs) to form a longitudinal structural constraint.

* Corresponding author. Academy of Medical Engineering and Translational Medicine, Tianjin University, Tianjin, 300072, China.
** Corresponding author.
E-mail addresses: S.J.Elliott@soton.ac.uk (S. Elliott), niguangjian@tju.edu.cn (G. Ni).
[1] contributed equally to this work.

https://doi.org/10.1016/j.crneur.2022.100045
Received 10 December 2021; Received in revised form 9 May 2022; Accepted 10 June 2022
Available online 20 June 2022

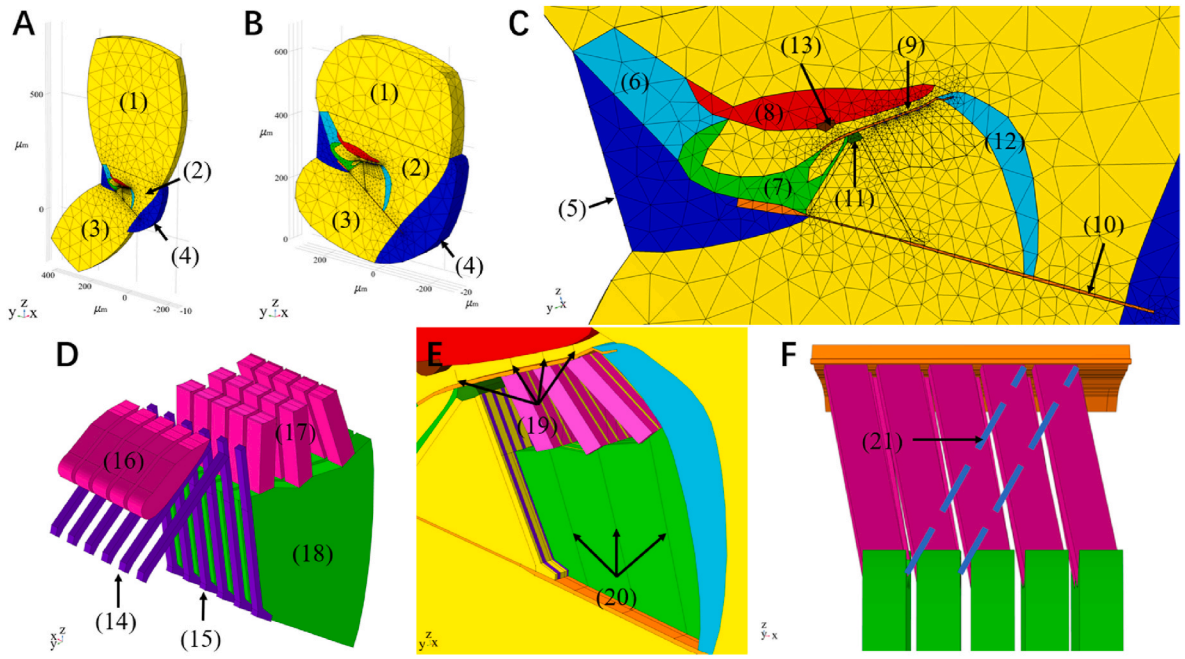

Fig. 1. Three-dimensional segmental models of the guinea pig cochlea. (A) The high-frequency model with a CF of 16 kHz. (B) The low-frequency model with a CF of 0.8 kHz. (C) Structure and mesh of the organ of Corti. (D) Discontinuous components in the organ of Corti. (E) Beam structures of some discontinuous components in the organ of Corti. (F) PhPs span 3 outer hair cells longitudinally. All structure names included in the model are numbered as follow: (1) Scala vestibuli, (2) Scala media, (3) Scala tympani, (4) Spiral ligament, (5) Spiral lamina, (6) Spiral limbus, (7) Inner sulcus cells, (8) Tectorial membrane, (9) Reticular lamina, (10) Basilar membrane, (11) Pillar cell head, (12) Hensen cells, (13) Hensen stripe, (14) Inter pillar cells, (15) Outer pillar cells, (16) Inter hair cells, (17) Outer hair cells, (18) Deiters cells, (19) Stereocilia, (20) Deiters rods, (21) Phalangeal processes. Yellow segments denote fluid elements, black and blue lines denote beam elements, and the rest denote solid elastic elements. (For interpretation of the references to colour in this figure legend, the reader is referred to the Web version of this article.)

(3) Including the physiological details of the organ of Corti to form a strong constraint between microstructures.
(4) Ability to simulate the active response of the cochlea.

However, most of the existing cochlear models cannot meet the above conditions. Traditional two-dimensional models cannot simulate the longitudinal movement of the organ of Corti (Cai and Chadwick, 2003; Cai et al., 2004; Ni et al., 2016; Steele and Puria, 2005). Beam models always need to simplify the geometry of the organ of Corti (Nam, 2014; Nam and Fettiplace, 2010), but three-dimensional models could reflect more detailed physiological structures (Zagadou et al., 2020). The "feedforward" models proposed by Steele et al. (1993, 1999) and Geisler and Sang (1995) reproduced many of the structural features but did not focus on producing the longitudinal vibration in the hotspot.

In this paper, we developed two three-dimensional segmented cochlear models, including detailed micro-physiological structures in the organ of Corti, corresponding to cochlear high- and low-frequency regions, respectively. These models included orthotropic material properties of some microstructures, the OHCs longitudinal tilt, the PhPs, and the longitudinal coupling between discontinuous structures. The superposition of the OC responses due to acoustic and OHCs excitation was used for calculating the active cochlear responses. The hotspot results simulated by the high-frequency model are compared with the experiments to verify the effectiveness. Similar results were obtained using the low-frequency model. Further, we analyzed the effect of viewing angle on the results. We then changed part of the excitation conditions and structure settings to illustrate the role and influence of some factors on the hotspot phenomenon.

Table 1
Continuity in the models.

Components (abbreviation)	Continuity	Components (abbreviation)	Continuity
Scala vestibuli (SV)	Yes	Hensen stripe	Yes
Scala media (SM)	Yes	Pillar cell head (PC)	Yes
Scala tympani (ST)	Yes	Outer pillar cell (OPC)	No
Spiral ligament	Yes	Inner pillar cell (IPC)	No
Spiral lamina (SLa)	Yes	Inner hair cell (IHC)	No
Spiral limbus	Yes	Outer hair cell (OHC)	No
Inner sulcus cells (ISC)	Yes	Stereocilia (St)	No
Tectorial membrane (TM)	Yes	Deiters cell (DC)	No
Reticular lamina (RL)	Yes	Deiters cell rod (DC rod)	No
Basilar membrane (BM)	Yes	Phalangeal processes (PhPs)	No
Hensen cell (HenC)	Yes		

2. Materials and methods

2.1. Model overview

Two three-dimensional guinea pig cochlea segmental models were built in COMSOL Multiphysics 5.6, including the detailed micro-physiological structures corresponding to cochlear low- and high-frequency regions, as shown in Fig. 1. The finite element method was used to deal with the complexity of the geometric structures in the cochlea. The models were built on the millimeter scale, and microstructures were on the micrometer scale.

The high-frequency model was drawn based on geometry data from Salt laboratory[2] corresponding to the position where the characteristic frequency is about 16 kHz, and the total thickness is 36 μm. The low-frequency model was drawn based on the existing two-dimensional model (Ni et al., 2016), corresponding to the position where the characteristic frequency is 0.8 kHz and the total thickness is 60 μm.

First, we constructed a high-frequency model to reproduce the

[2] Alec Salt's laboratory: http://oto2.wustl.edu/cochlea/(Last viewed June 4, 2016).

hotspot phenomenon in the experiments. The measured region by Cooper et al. (2018) corresponds to characteristic frequencies from about 20 kHz to 40 kHz. According to the gerbil cochlea frequency tonotopy (Muller, 1996), this frequency range corresponds to a position range 10%–23% of the total gerbil cochlea length away from the base. For the guinea pig cochlea, 10%–23% of the total length away from the base corresponds to a characteristic frequency range of 14.3 kHz–27 kHz (Greenwood, 1990; Ni et al., 2017; Nuttall et al., 1999). Therefore, we built our high-frequency model with a characteristic frequency of 16 kHz. Referring to the data of Salt laboratory and Fernandez (1952), the scala vestibuli (SV) height was 463 μm, the scala media (SM) height was 77 μm, the scala tympani (ST) width was 318 μm, and the BM width was 110 μm in the high-frequency model. The average length of OHCs in the 16 kHz model was 23 μm, consistent with estimations (Kelly, 1989).

Then we built the low-frequency model based on the 2D model by Ni et al. (2016). The longitudinal continuity of microstructures in the cochlea was treated differently in the model, as listed in Table 1. The scala fluid and part of the solid structures are continuously distributed (Kikuchi et al., 1995). They were stretched with the same length along the longitudinal direction as the overall model, 60 μm. A Thermoviscous-Acoustics condition, used to solve linearized Navier–-Stokes and Fourier heat equations, was set for the fluids, but heat transmission was neglected, and only the fluid-flow equations of momentum in the frequency domain were considered here, as

$$i\omega\rho_f \mathbf{u}_f = \nabla\cdot\left[-p_{va}\mathbf{I} + \mu\left(\nabla\mathbf{u}_f + (\nabla\mathbf{u}_f)^{T}\right) + \left(\mu_B - \frac{2}{3}\mu\right)(\nabla\cdot\mathbf{u}_f)\mathbf{I}\right] = 0 \quad (1)$$

where $\mathbf{u}_f$ is the velocity field (the effects of gravity are neglected), ρ_f and p_{va} are the fluid density and viscoacoustic fluid pressure. μ and μ_B are the dynamic and bulk viscosity, respectively. $\mathbf{I}$ represents the unity matrix, and i, ∇, and ω are the imaginary unit, differential operator, and angular frequency, respectively.

The pillar cells, hair cells, stereocilia, DCs, and Deiters rods were arranged at a specific interval along the longitudinal direction (Raphael and Altschuler, 2003). The pillar and hair cells were approximated as cylinders in the *y*-*z* plane with thickness of 3.2 μm and 8.4 μm in the longitudinal direction (Karavitaki and Mountain, 2007). The outer hair cells were set to be inclined 10° in the longitudinal direction, referring to the average measurement mice (Soons et al., 2015) because the guinea pig value is unknown yet. The influence of different OHCs tilt angles on the results was discussed. The Deiters cells were assigned the same longitudinal thickness with the outer hair cells, which were close to measurement (Karavitaki and Mountain, 2007). The W or V-shaped hair bundles at the top of the hair cells were simplified into the tallest row of stereocilia. The stereocilia of OHCs were connected to the TM bottom, while the stereocilia of IHCs were not (Lim, 1986). The stereocilia were all constructed with Timoshenko beams and located in the middle layer of each segment along the longitudinal direction. The diameters of the stereocilia, the PhPs, and the DC rods were set to be 0.2 μm, 1 μm, and 1 μm, respectively (Bohnke et al., 1999; Nam and Fettiplace, 2010). The gaps between the discontinuous structures were filled with fluid, and discontinuous structures were entirely wrapped by fluid.

The PhPs were modeled with beam element, and one end was connected to the bottom of OHCs, and the top of Deiters rods, forming a Y-shaped structure. The other end of the PhPs was connected to the bottom of the reticular lamina. The average length of OHCs in the 0.8 kHz model is about 45 μm, consistent with estimations (Kelly, 1989). The experimental results show that the angle of OHCs and PhPs in the guinea pig cochlea is about 35° (Zetes et al., 2012). Based on the trigonometric relationship between the structures, the longitudinal spacing of PhPs is about 3 OHCs.

Table 2
Material properties of orthotropic materials in the model.

Components	Parameter	Low-frequency model	High-frequency model
Tectorial membrane	Young's modulus [Pa]	E_{XX}: 4e3 E_{YY}: 4e4 E_{ZZ}: 4e4	E_{XX}: 1.2e5 E_{YY}: 4.8e6 E_{ZZ}: 4.8e6
	Shear modulus [Pa]	G_{XY}: 2e3 G_{YZ}: 2e4 G_{XZ}: 2e3	G_{XY}: 6e4 G_{YZ}: 2.4e6 G_{XZ}: 6e4
	Poisson's ratio	V_{XY}: $\frac{1}{10}\left(\frac{1}{2}-\frac{E_{YY}}{6K}\right)$ V_{YZ}: $\frac{1}{10}\left(\frac{1}{2}-\frac{E_{YY}}{6K}\right)$ V_{XZ}: $\frac{1}{2}-\frac{E_{YY}}{6K}$	V_{XY}: $\frac{1}{40}\left(\frac{1}{2}-\frac{E_{YY}}{6K}\right)$ V_{YZ}: $\frac{1}{40}\left(\frac{1}{2}-\frac{E_{YY}}{6K}\right)$ V_{XZ}: $\frac{1}{2}-\frac{E_{YY}}{6K}$
Reticular lamina	Young's modulus [Pa]	E_{XX}: 3e8 E_{YY}: 3e9 E_{ZZ}: 3e9	E_{XX}: 9e9 E_{YY}: 3.6e11 E_{ZZ}: 3.6e11
	Shear modulus [Pa]	G_{XY}: 1e8 G_{YZ}: 1e9 G_{XZ}: 1e8	G_{XY}: 3e9 G_{YZ}: 1.2e11 G_{XZ}: 3e9
	Poisson's ratio	V_{XY}: $\frac{1}{10}\left(\frac{1}{2}-\frac{E_{YY}}{6K}\right)$ V_{YZ}: $\frac{1}{10}\left(\frac{1}{2}-\frac{E_{YY}}{6K}\right)$ V_{XZ}: $\frac{1}{2}-\frac{E_{YY}}{6K}$	V_{XY}: $\frac{1}{40}\left(\frac{1}{2}-\frac{E_{YY}}{6K}\right)$ V_{YZ}: $\frac{1}{40}\left(\frac{1}{2}-\frac{E_{YY}}{6K}\right)$ V_{XZ}: $\frac{1}{2}-\frac{E_{YY}}{6K}$
Basilar membrane	Young's modulus [Pa]	E_{XX}: 6e5 E_{YY}: 6e6 E_{ZZ}: 6e6	E_{XX}: 1.8e7 E_{YY}: 7.2e8 E_{ZZ}: 7.2e8
	Shear modulus [Pa]	G_{XY}: 2e5 G_{YZ}: 2e6 G_{XZ}: 2e5	G_{XY}: 6e6 G_{YZ}: 2.4e8 G_{XZ}: 6e6
	Poisson's ratio	V_{XY}: $\frac{1}{10}\left(\frac{1}{2}-\frac{E_{YY}}{6K}\right)$ V_{YZ}: $\frac{1}{10}\left(\frac{1}{2}-\frac{E_{YY}}{6K}\right)$ V_{XZ}: $\frac{1}{2}-\frac{E_{YY}}{6K}$	V_{XY}: $\frac{1}{40}\left(\frac{1}{2}-\frac{E_{YY}}{6K}\right)$ V_{YZ}: $\frac{1}{40}\left(\frac{1}{2}-\frac{E_{YY}}{6K}\right)$ V_{XZ}: $\frac{1}{2}-\frac{E_{YY}}{6K}$

2.2. Boundary conditions

In this work, both models used the same boundary conditions. The two ends of the basilar membrane were connected with the spiral lamina and the spiral ligament. The boundary conditions are more complicated and depend on the adjacent tissue and fiber structure. Ni et al. (2013) showed that boundary conditions at both ends of the basilar membrane have little effect on the fluid coupling and coupled response. Therefore, we fixed the spiral ligament and spiral lamina, corresponding to the tightening of the basilar membrane on both ends, which is consistent with Steele and Puria (2005) and Ni et al. (2016).

The solid surface was set as a continuous periodic condition to simulate their movement under a periodic arrangement. This boundary condition makes the displacement of the two sides of the boundary always equal, as,

$$u(x_d) = u(x_s), \quad (2)$$

where u is the displacement of solid, x_d and x_s are corresponding positions on both sides of the model. The effect of this boundary condition was discussed in Appendix I. The fluid was set to be no-stress boundary

Table 3
Material properties of isotropic materials in the model.

Components	Low-frequency model Young's modulus [Pa]	High-frequency model Young's modulus [Pa]
Spiral ligament	1e9	1.2e11
Spiral lamina	1e9	1.2e11
Spiral limbus	1e6	1.2e8
Inner sulcus cell	3e3	3.6e5
Hensen stripe	3e3	3.6e5
Hensen cell	3e3	3.6e5
Deters cell	3e3	3.6e5
Deiters cell rod	1e8	1.2e10
Pillar cell head	1e7	1.2e9
Outer pillar cell	1e8	1.2e10
Inner pillar cell	1e8	1.2e10
Inner hair cell	3e3	3.6e5
Outer hair cells	1e4	1.2e6
Stereocilia	1e5	1.2e7
Phalangeal processes	1e8	1.2e10

so that the total surface stress was zero, as,

$$\left[-p_t\mathbf{I}+\mu\left(\nabla\mathbf{u}_t+(\nabla\mathbf{u}_t)^{\mathrm{T}}\right)-\left(\frac{2\mu}{3}-\mu_{\mathrm{B}}\right)(\nabla\mathbf{u}_t)\mathbf{I}\right]\mathbf{n}=0 \tag{3}$$

where p_t is the total acoustic pressure, $\mathbf{u}_t$ is the total acoustic velocity, μ is the dynamic viscosity, μ_B is the bulk viscosity, $\mathbf{I}$ is the second-order identity tensor, and $\mathbf{n}$ is the normal direction. The no-stress boundary condition can simulate the longitudinal pressure release of the fluid when the organ of Corti moves. For example, when the organ of Corti moves, the volume of fluid in the SV and ST will change, which will change the pressure. If there were no such setting, this pressure change would restrict the movement of the organ of Corti. The effects of this boundary condition are discussed in Appendix II.

All contact surfaces between fluid and solid in the models were set as Thermoviscous Acoustic-Structure Boundary, which includes the coupling between the discontinuous structure and the fluid inside the organ of Corti. This coupling is described in the frequency domain as,

$$u_{\mathrm{t,fluid}}=i\omega u_{\mathrm{solid}} \tag{4}$$

where $u_{\mathrm{t,fluid}}$ is the total fluid velocity, and u_{solid} is the solid displacement. This coupling ensures stress being continuous across the fluid-structure interface. Spatial continuity of displacement is enforced at the connection nodes between the beam and solid elements by,

$$\mathbf{u}_b=\mathbf{u}_s, \tag{5}$$

where $\mathbf{u}_b$ and $\mathbf{u}_s$ are the displacement of beam and solid, respectively. Since the beam elements in finite element models do not feature actual surfaces to interact with the surrounding domain, fluid–structure interaction conditions do not apply to beams.

2.3. Material properties

Material properties of each structure are listed in Table 2 and Table 3. To adjust the resonance frequency to be consistent with the defined characteristic frequency, the stiffness of some components was adjusted to be consistent with measurements and existed models (Cai and Chadwick, 2003; Steele and Puria, 2005; Zwislocki and Cefaratti, 1989).

Orthotropic materials were used for TM, RL, and BM. Liu and White (2008) showed that the orthotropy ratio was 10 at the upper-middle turn of the cochlea and 68 at the base. They pointed out that the value may vary along the length of the cochlea. The guinea pig cochlea was 18.5 mm long, and the characteristic frequency at the base, f_B, was 44 kHz (Fernandez, 1952). The characteristic frequency of the guinea pig cochlea exponentially decreases from the base to the apex (Greenwood, 1990; Nuttall et al., 1999), as

$$\mathrm{CF}(x)=f_B\,e^{-x/l}, \tag{6}$$

where x is the distance to the base, and l is the characteristic frequency distribution scale, which was set to 3.8 mm in our work. The location with a characteristic frequency of 0.8 kHz was then calculated to be about 15.2 mm away from the base, close to the cochlea upper-middle turn. Meanwhile, the 16 kHz position is 3.8 mm away from the base. Therefore, the orthotropy ratio was set to 10 for the low-frequency model and 40 for the high-frequency model.

The density of all components in the model was the same as water, 1000 kg/m^3. Poisson's ratio, ν, had a linear relationship with Young's modulus, E, as $\nu = 1/2\text{-}E/6/K$, where $K = 1$ GPa. The damping was included in the stiffness matrix as a loss factor of 0.1. The fluid was incompressible with a dynamic viscosity of 1 mPa·s.

2.4. Mesh

The organ of Corti includes complex three-dimensional structures. The mesh of the model was adjusted to ensure the quality of the elements, as shown in Fig. 1. One-dimensional beam elements were used for the stereocilia, phalangeal processes, and Deiters rods. All other structures were meshed with tetrahedron elements. The organ of Corti and the fluid area nearby were meshed densely, and the SV, SM, and ST areas were meshed relatively loosely. The low-frequency model had 36,123 solid elements, 184 beam elements, and 39,106 fluid elements. The high-frequency model had 34,572 solid elements, 171 beam elements, and 38,292 fluid elements. The quadratic elements were selected for solid and fluid. The axial displacement and twist are represented by linear shape functions in the beam elements, while a cubic shape function represents the bending.

2.5. Stimulation of active response

The active response was calculated by superimposing acoustic and OHCs excitations to simulate the movement of the organ of Corti in the

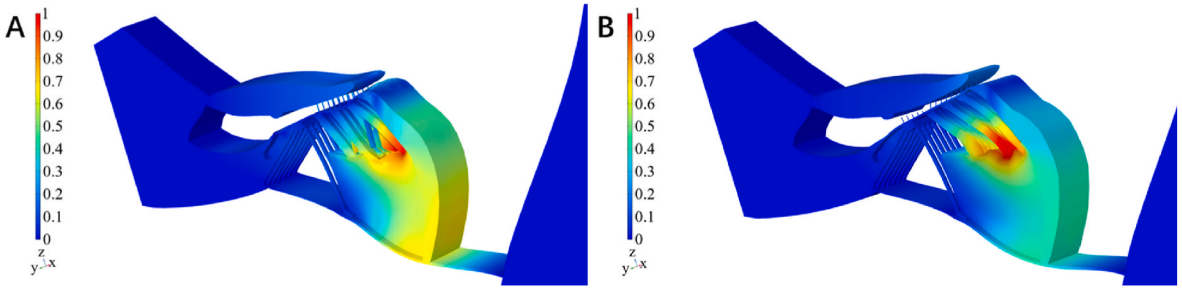

Fig. 2. The active responses calculated based on (A) the high-frequency model and (B) the low-frequency model. The amplitudes were normalized with respect to the maximum value, and the deformation was magnified by 300 and 5 times for better visualization.

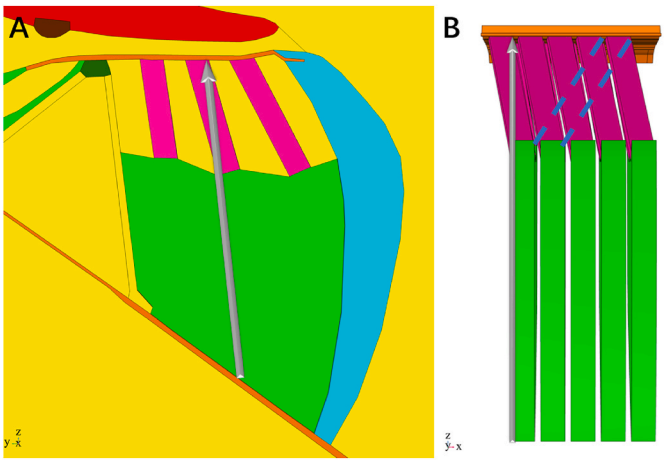

Fig. 3. Defined path, marked with a gray arrow, for calculating longitudinal displacements of different components in the organ of Corti. (A) Transverse view. (B) Longitudinal view.

living cochlea. First, a sinusoidal pressure difference was uniformly applied to the BM to simulate the excitation when the sound propagates along the cochlea. Under the action of acoustic excitation, RL and TM will undergo shearing motion, which determines the magnitude of the load at both ends of the OHCs. The OHC force was calculated as follow (Geleoc et al., 1997; Murakoshi et al., 2015)

$$F_{OHC}\left(x\right) = \frac{F_{\max}}{1 + e^{\alpha_1(x_1 - x)}\left(1 + e^{\alpha_2(x_2 - x)}\right)} \tag{7}$$

where F_{max} is the maximum load that can be generated at both ends of the OHC, set to 155 nN, x is the shear displacement of RL and TM, x_1 and x_2 are the displacements, at which the setpoints of transition between states were set to 0.092 nm^{-1} and 0.038 nm^{-1} α_1 and α_2 are the displacement sensitivities of the transitions, set to 8.2 nm and 49 nm (Geleoc et al., 1997).

3. Results

3.1. Hotspots in OHCs and DCs area

First, we calculated the active response of the organ of Corti based on the high- and low-frequency model, as shown in Fig. 2. When the BM moves towards the ST, the shearing movement between the RL and TM causes OHCs to elongate. The location with the most significant response is close to OHCs and DCs, as observed in the experiments (Cooper et al., 2018).

As shown in Fig. 3, a path was defined, similar to the definition in the experiment (Cooper et al., 2018), to compare the model results with the experiment. This path starts from the BM, passes through the DCs and OHCs area, and extends to the bottom of the RL. The intersection between OHCs and Deiters cells that the path passes through connects PhPs. The longitudinal displacement amplitude was calculated along the defined path using the two models, as shown in Fig. 4. It can be seen that the longitudinal displacement amplitude of the two models reaches the maximum near the junction of DCs and OHCs, while the response close to BM and RL is small. Furthermore, the phase of DCs and OHCs is different from BM, consistent with the measured results in the experiment. Our model demonstrates how hotspot vibrations could be observed in the low-frequency region. It can be seen that the response amplitude of the low-frequency model is greater than that of the high-frequency model when driven by the same stimuli.

3.2. The effect of viewing angle on the hotspot

In the experimental study, the effect of different viewing angles on the results was predicted (Cooper et al., 2018). Based on the possible complex motion of the BM, Cooper et al. speculated: "Under the effect of the traveling wave, the phase of the hotspot will lead the BM when observing towards the apex and lag the BM when observing towards the base." They then observed a similar phenomenon in their experiments.

Based on the high-frequency model, we also explored the influence of viewing angles on the hotspot. Referring to the method of Cooper et al. (2018), the viewing angle toward the cochlear apex was defined as "negative", and toward the base as "positive", as shown in Fig. 5. Along with the two viewing angles, the calculated results of different deviation angles are shown in Fig. 6. It can be seen that under the positive viewing angle, the results are in good agreement with the experimental results, and the hotspot phase lags to the BM. A similar phenomenon is also shown from the negative viewing angle, but the hotspot phase leads to the BM. Although the segmental model used in this study cannot include the effect of the traveling wave, the hotspot phase leading or lagging to the BM is still observed at different viewing angles. In this way, our results confirmed Cooper et al. predictions (4) and (5) (See supplementary information in Cooper et al. (2018). Since the deviation from

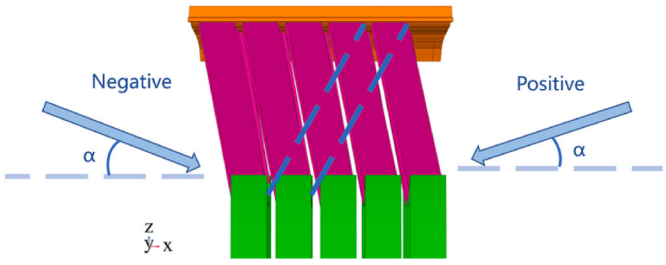

Fig. 5. Sketch of different viewing angles to the longitudinal direction.

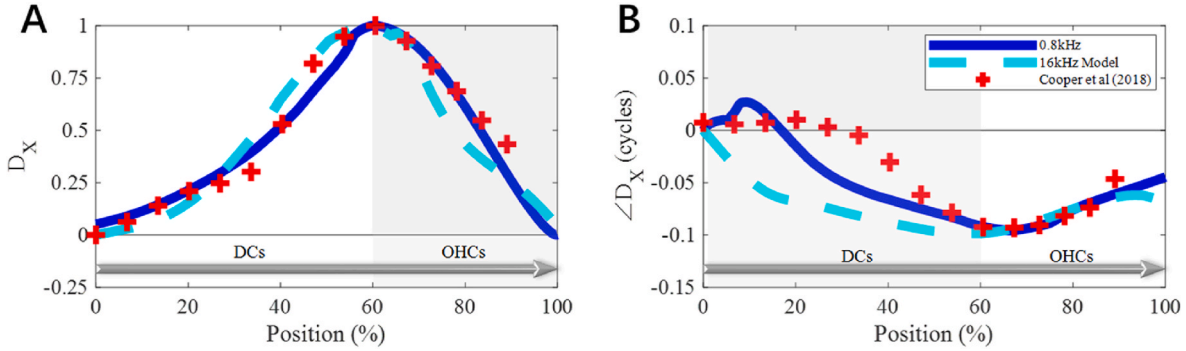

Fig. 4. (A) The amplitude (A) and phase (B) of longitudinal displacement along the defined path. The amplitudes were processed with the min-max normalization method. The horizontal axis shows the percentage of the distance along the defined path.

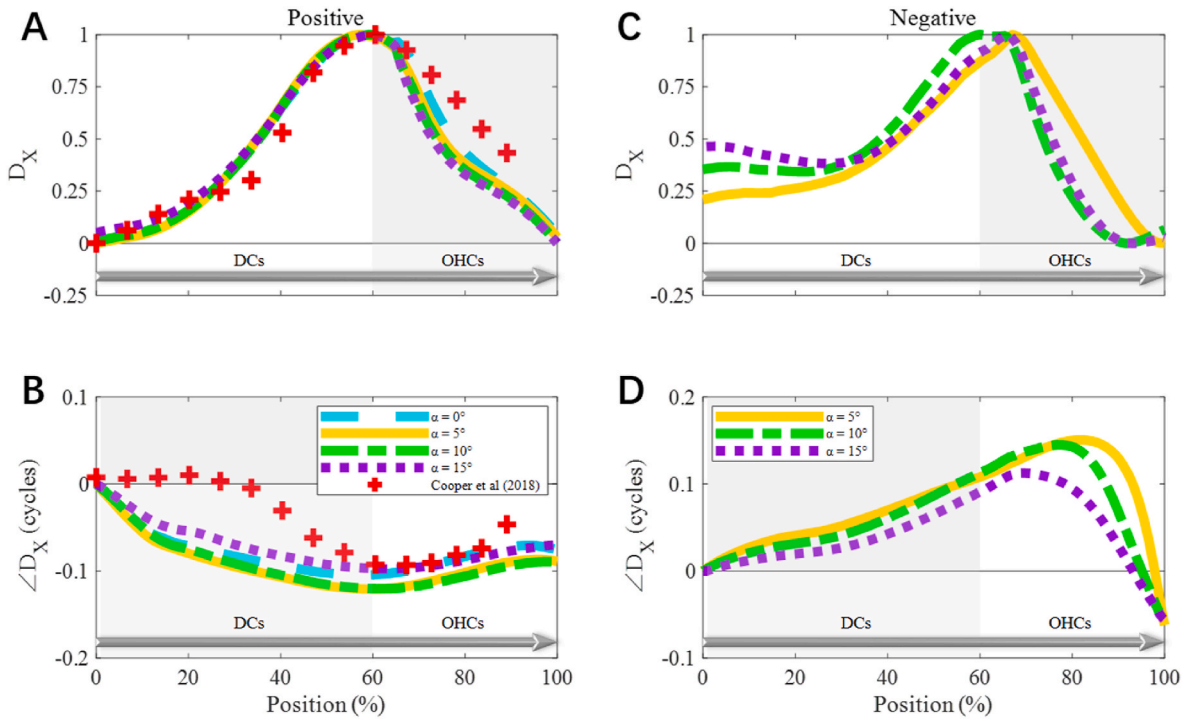

Fig. 6. The positive (A, B) and negative (C, D) viewing angles, the amplitude (A, C), and phase (B, D) of longitudinal displacement along the defined path. The amplitudes were processed with the min-max normalization method. The phase results are calculated with reference to the position closest to the BM. The horizontal axis shows the percentage of the distance along the defined path.

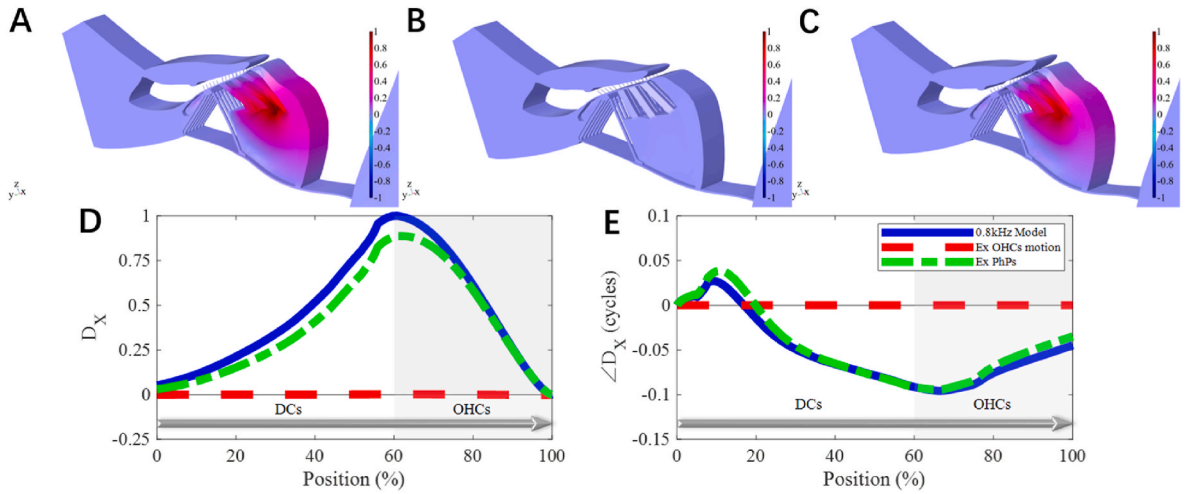

Fig. 7. Deformation when (A) the model is fully active, (B) OHCs motility is excluded, and (C) PhPs are eliminated. The longitudinal displacements in (A), (B), and (C) are normalized, and the deformation is magnified 5 times (A, C) and 100 times (B) for better visualization. The amplitudes were processed with the min-max normalization method. The (D) amplitude and (E) phase of DCs and OHCs longitudinal displacement. The amplitudes were normalized with respect to the results of the 0.8 kHz model. The horizontal axis shows the percentage of the distance along the defined path.

different angles has little effect on the results, the resulst below focus on calculating the properties of the hotspot response using the positive viewing angle (specifically at $\alpha = 0$).

3.3. Contributions of OHCs somatic motion and PhPs constraints to the hotspot

The experimental hypothesis is that the hotspot response is triggered by the activity of OHCs and is related to integrated structural constraints (Cooper et al., 2018). We recalculated the movement of the organ of Corti when PhPs or OHCs excitation was excluded, as shown in Fig. 7. It can be seen that when the excitation of OHCs is stopped, the longitudinal deformation will disappear. When the PhPs are neglected, hotspot response amplitude is slightly decreased. It can be seen that the OHCs activity play an essential role in producing hotspot, and the existence of PhPs has further promoted the occurrence of this phenomenon.

3.4. The effect of OHCs tilt angle on the hotspot

In our model, the OHCs are inclined 10° in the longitudinal direction. Existing studies have shown that the inclination angle of OHCs in different species is different. For example, the average inclination angle

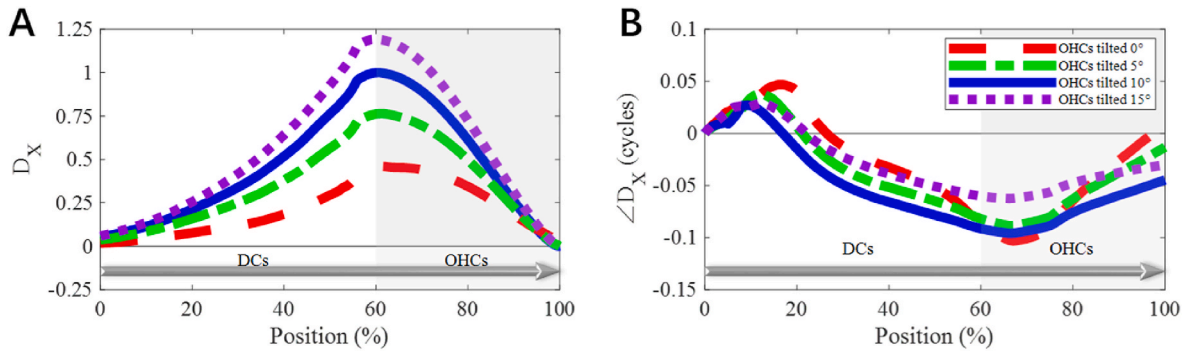

Fig. 8. The amplitude (A) and phase (B) of DCs and OHCs longitudinal displacement when OHCs are inclined at different angles in the longitudinal direction. The amplitudes were normalized with respect to results when OHCs tilt 10°. The horizontal axis shows the percentage of the distance along the defined path.

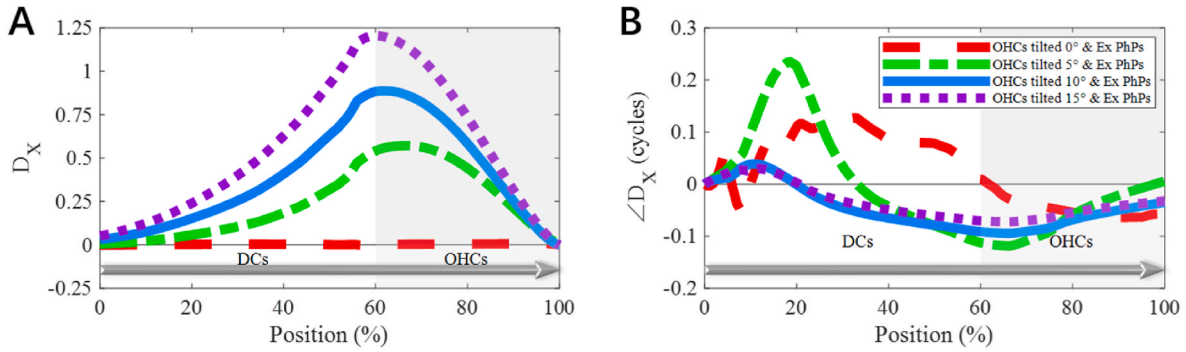

Fig. 9. The amplitude (A) and (B) phase of DCs and OHCs longitudinal displacement when PhPs are excluded and OHCs inclined at different angles in the longitudinal direction. The amplitudes were normalized with respect to results when the OHCs tilted 10°. The horizontal axis shows the percentage of the distance along the defined path.

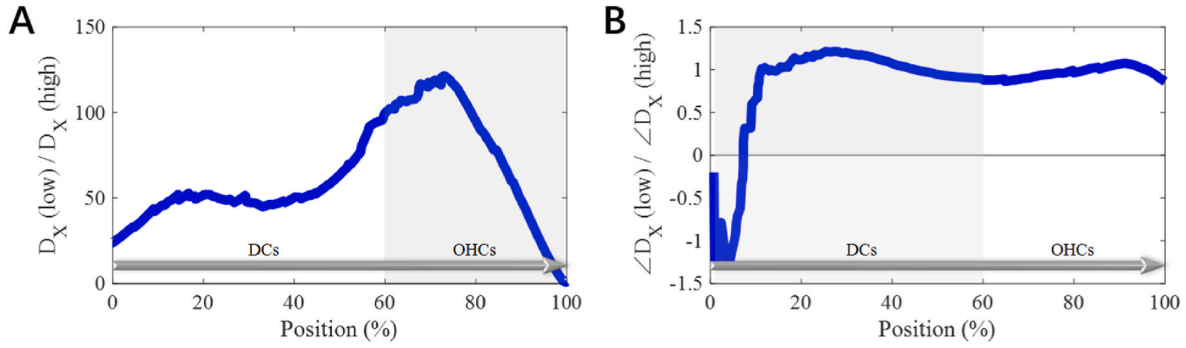

Fig. 10. Comparison of DCs and OHCs (A) longitudinal displacement and (B) phase calculated with the low- and high-frequency models. The horizontal axis shows the percentage of the distance along the defined path.

of gerbils is 5°, and that of chinchilla is 15° (Yoon et al., 2011). It was also shown that even in the same species, the tilt angles at different positions of the cochlea are different. For example, the tilt range in mice is from 5° to 15° (Soons et al., 2015). Moreover, some results showed that OHCs and RL occasionally tend to be perpendicular (Raphael et al., 1991; Soons et al., 2015).

To explore the influence of different tilt angles on the hotspot response, we changed the OHCs to be inclined 0°, 5°, 10°, and 15° longitudinally, as shown in Fig. 8. The greater the tilt angle of the OHCs along the longitudinal direction, the greater hotspot amplitude. It is worth noting that when the OHCs are not tilted in the longitudinal direction, the result also shows evident hotspot vibration. This may indicate that PhPs played a more critical role in this phenomenon.

We also explored the role of PhPs on hotspots when the OHCs inclined at different angles, as shown in Fig. 9. If there were no PhPs, hotspot vibration will still occur when OHCs are tilted longitudinally, even if the tilt angle is slight. But when the OHCs are not inclined in the longitudinal direction, the hotspot will disappear without PhPs.

3.5. The effect of PhPs longitudinal span on the hotspot

We first compared the hotspot responses of the high- and low-frequency models with the same PhPs span, 3 OHCs, as shown in Fig. 10. It can be seen that the response amplitude of the low-frequency model is much greater than that of the high-frequency model.

Existing studies have observed geometric parameters in different species and found some differences. For example, the longitudinal span of PhPs is 2 OHCs spacing in gerbils (Karavitaki and Mountain, 2007), 3 in mouse (Soons et al., 2015), and 4–5 in mole rat (Raphael et al., 1991). Moreover, the longitudinal spacing of OHCs in these species is close,

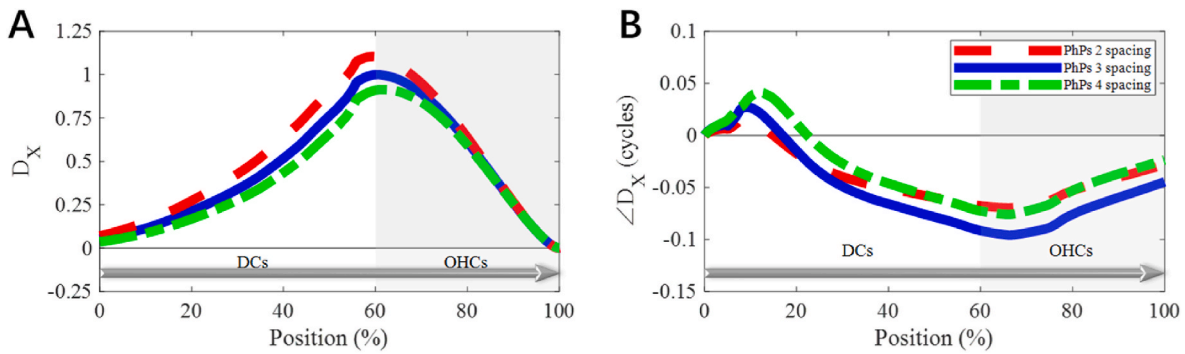

Fig. 11. The amplitude (A) and phase (B) of DCs and OHCs longitudinal displacement when PhPs span different spacing along the longitudinal direction. The amplitudes were normalized with respect to results when PhPs span 3 OHCs. The horizontal axis shows the percentage of the distance along the defined path.

with a distance of about 10 μm. Therefore, we used the guinea pig model to study the effect of different longitudinal spans of PhPs on the hotspot response, as shown in Fig. 11. It can be seen that the hotspot response is more significant when the PhPs span is shorter.

4. Conclusion and discussion

Two three-dimensional models of the organ of Corti were developed, describing the high- and low-frequencies regions in the cochlea, which are not a simple spatial stretching but included several different continuity conditions based on the natural physiological structure. Although the model constructed using beam elements could reduce the amount of calculation, it cannot describe the local response of the organ of Corti in detail. A three-dimensional model allows the simulation of the integrated spatial coupling between solid and fluid. Compared with the two-dimensional model, the three-dimensional model considers the longitudinal tilt of OHCs and the structure of PhPs, which makes it possible to study the influence of these factors on the hotspot phenomenon.

It should be noted that even without the traveling wave, our model still validated the predictions (4) and (5) mentioned above and reproduced similar phenomena to experiments, including the vibrational morphology of the hotspot and phase lead or lag depending on the viewing angle. Therefore, we hypothesize that the hotspot is a locally originated phenomenon in the cochlea, but the traveling wave further enhances the response of the hotspot to low-frequency excitation.

When the OHCs activity was excluded, the longitudinal deformation of the OHCs and DCs area was significantly reduced, confirming that the activity of OHCs induces the hotspot vibration (Dewey et al., 2021). In addition, the results show that the longitudinal structural constraints of PhPs also slightly contribute to the formation of the hotspot. Our results confirm that the hotspot occurs in both high-frequency and low-frequency regions.

In summary, the movement of OHCs triggers the hotspot and the PhPs structural constraints promote this phenomenon, which supports the experimental hypothesis (Cooper et al., 2018). The hotspot phenomenon occurs regardless of the tilt angle of the OHCs, a larger tilt angle induces a larger amplitude. When OHCs are not inclined, the structural constraints of PhPs become the main reason and a shorter PhPs span will induce a larger hotspot amplitude.

CRediT authorship contribution statement

Junpei Liu: contributed to the conception and design of the work, Writing – original draft, drafting and revising the manuscript. participated in modeling work. All authors agreed to submit the manuscript in its current state and agree to be accountable for all aspects of the work. **Yanru Bai:** Conceptualization, contributed to the conception and design of the work, Writing – original draft, drafting and revising the manuscript. and participated in modeling work. All authors agreed to submit the manuscript in its current state and agree to be accountable for all aspects of the work. **Qianli Cheng:** participated in modeling work, and All authors agreed to submit the manuscript in its current state and agree to be accountable for all aspects of the work. **Shu Zheng:** participated in modeling work. All authors agreed to submit the manuscript in its current state and agree to be accountable for all aspects of the work. **Stephen Elliott:** contributed to the conception and design of the work, Writing – original draft, drafting and revising the manuscript. All authors agreed to submit the manuscript in its current state and agree to be accountable for all aspects of the work. **Guangjian Ni:** Conceptualization, contributed to the conception and design of the work, Writing – original draft, drafting and revising the manuscript. participated in modeling work. All authors agreed to submit the manuscript in its current state and agree to be accountable for all aspects of the work.

Declaration of competing interest

The authors declare that they have no known competing financial interests or personal relationships that could have appeared to influence the work reported in this paper.

Acknowledgments

The work was supported by grants from the National Natural Science Foundation of China (81971698) and the Beijing-Tianjin-Hebei Basic Research Cooperation Project (18JCZDJC45300).

Appendix I. Effects of Periodic Condition

Periodic conditions were assumed along the longitudinal solid side boundaries. To verify the effect of periodic conditions on the hotspot response, we extended the existing model longitudinally to 60 μm, 180 μm, 300 μm, and 420 μm, that is, the original model extended the same length along both sides of the longitudinal direction, as shown in Fig. I.A, and recalculated the movement of the organ of Corti. It can be seen from Fig. I.B that the movement of the organ of Corti has not changed after the model is extended. Fig. I.C and D show no change in the hotspot response after the model is extended.

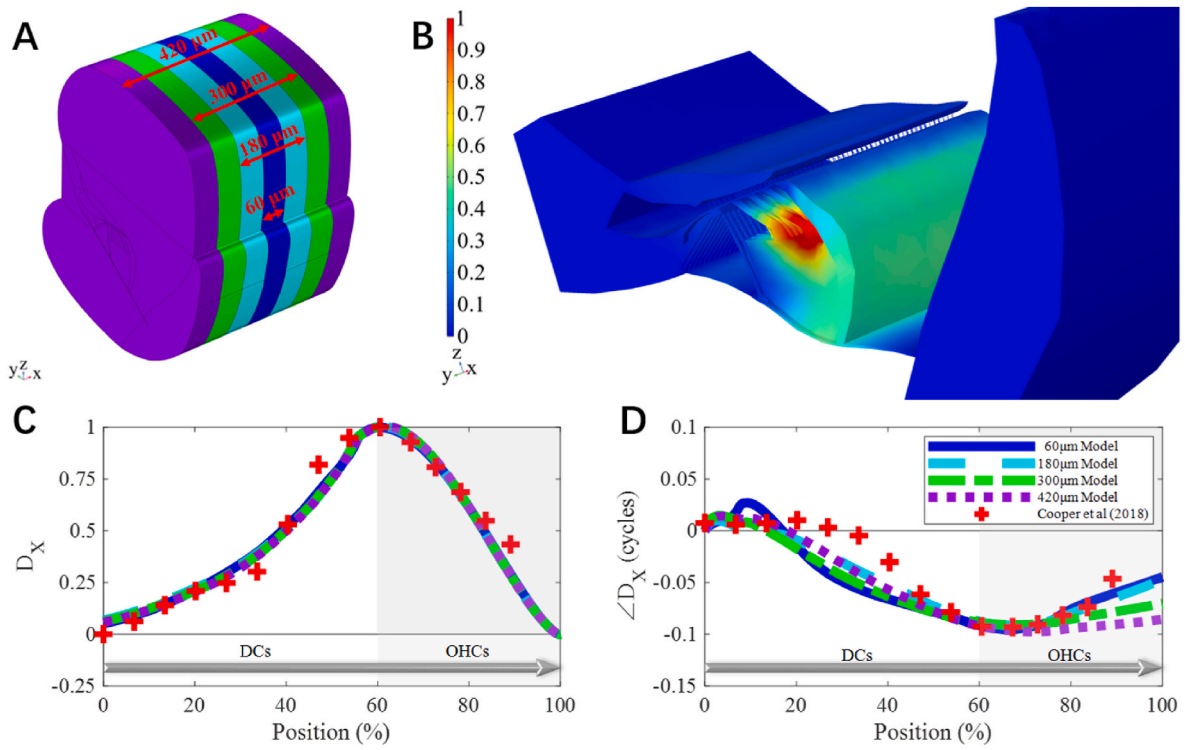

Fig. I. (A) Models with different lengths in the longitudinal direction. The blue denotes 60 μm long (the original length), red 180 μm, green 300 μm, and purple 420 μm. (B) The active response of the organ of Corti when the model was extended to 420 μm. The amplitudes were processed with the min-max normalization method. The amplitude (C) and phase (D) of DCs and OHCs longitudinal displacement when the model is extended with different lengths. The amplitudes were normalized with respect to results when the model was 60 μm thick in the longitudinal direction. The horizontal axis shows the percentage of the distance along the defined path.

Appendix II. Effects of no-stress condition

The two sides of the fluid area along the longitudinal direction of the model were set as no stress conditions. Under the existing model settings, loads of different frequencies are applied to the bottom of the BM. The movement of the BM is shown in Fig. II. The result showed a steady upward trend from low to high frequency, reaching the maximum value at 0.8 kHz, and rapidly decreasing. The model can simulate the response trend in the cochlea. But when the no-stress condition is eliminated, this trend does not appear.

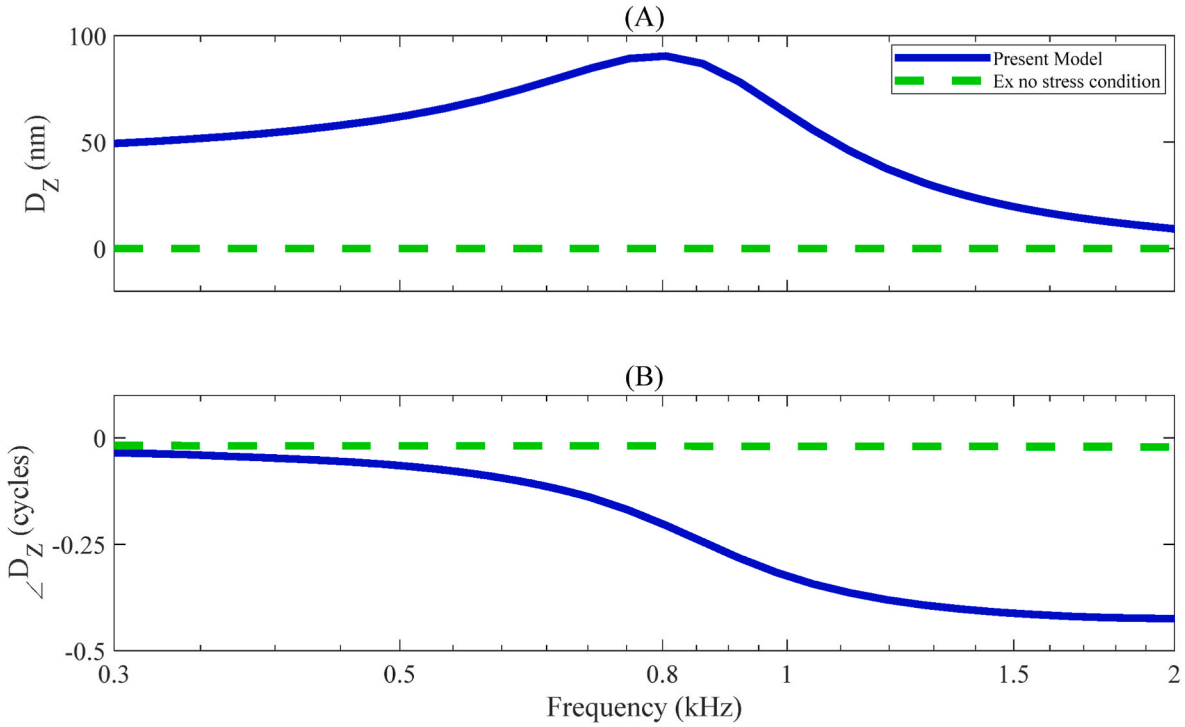

Fig. II. (A) Amplitude and (B) phase of the BM vertical displacement with and without no-stress conditions.

Appendix A. Supplementary data

Supplementary data to this article can be found online at https://doi.org/10.1016/j.crneur.2022.100045.

References

Bohnke, F., von Mikusch-Buchberg, J., Arnold, W., 1999. Active nonlinear mechanics of the organ of Corti including the stereocilia-tectorial membrane complex. ORL J. Oto-Rhino-Laryngol. its Relat. Specialties 61 (5), 311–317. https://doi.org/10.1159/000027689.

Cai, H.X., Chadwick, R., 2003. Radial structure of traveling waves in the inner ear. SIAM J. Appl. Math. 63 (4), 1105–1120. https://doi.org/10.1137/s0036139901388957. Pii s0036139901388957.

Cai, H.X., Shoelson, B., Chadwick, R.S., 2004. Evidence of tectorial membrane radial motion in a propagating mode of a complex cochlear model. Proc. Natl. Acad. Sci. U. S.A. 101 (16), 6243–6248. https://doi.org/10.1073/pnas.0401395101.

Cooper, N.P., Vavakou, A., van der Heijden, M., 2018. Vibration hotspots reveal longitudinal funneling of sound-evoked motion in the mammalian cochlea. Nat. Commun. 9 (12), 3054. https://doi.org/10.1038/s41467-018-05483-z.

Dewey, J.B., Altoe, A., Shera, C.A., Applegate, B.E., Oghalai, J.S., 2021. Cochlear outer hair cell electromotility enhances organ of Corti motion on a cycle-by-cycle basis at high frequencies in vivo. Proc. Natl. Acad. Sci. U.S.A. 118 (43), e2025206118 https://doi.org/10.1073/pnas.2025206118/-/DCSupplemental.

Fallah, E., Strimbu, C.E., Olson, E.S., 2021. Nonlinearity of intracochlear motion and local cochlear microphonic: Comparison between guinea pig and gerbil. Hear. Res. 405, 108234 https://doi.org/10.1016/j.heares.2021.108234.

Fernandez, C., 1952. Dimensions of the cochlea (Guinea pig). J. Acoust. Soc. Am. 24 (5), 519–523. https://doi.org/10.1121/1.1906929.

Geisler, C.D., Sang, C., 1995. A cochlear model using feed-forward outer-hair-cell forces. Hear. Res. 86 (1–2), 132–146. https://doi.org/10.1016/0378-5955(95)00064-b.

Geleoc, G.S., Lennan, G.W., Richardson, G.P., Kros, C.J., 1997. A quantitative comparison of mechanoelectrical transduction in vestibular and auditory hair cells of neonatal mice. Proc. Biol. Sci. 264 (1381), 611–621. https://doi.org/10.1098/rspb.1997.0087.

Greenwood, D.D., 1990. A cochlear frequency-position function for several species–29 years later. J. Acoust. Soc. Am. 87 (6), 2592–2605. https://doi.org/10.1121/1.399052.

He, W.X., Kemp, D., Ren, T.Y., 2018. Timing of the reticular lamina and basilar membrane vibration in living gerbil cochleae, 17 Elife 7, e37625. https://doi.org/10.7554/eLife.37625.

Karavitaki, K.D., Mountain, D.C., 2007. Imaging electrically evoked micromechanical motion within the organ of corti of the excised gerbil cochlea. Biophys. J. 92 (9), 3294–3316. https://doi.org/10.1529/biophysj.106.083634.

Kelly, J.P., 1989. Cellular organization of the Guinea pig's cochlea. Acta Otolaryngol. Suppl. 467, 97–112.

Kikuchi, T., Kimura, R.S., Paul, D.L., Adams, J.C., 1995. Gap junctions in the rat cochlea: immunohistochemical and ultrastructural analysis. Anat. Embryol. 191 (2), 101–118. https://doi.org/10.1007/bf00186783.

Lim, D.J., 1986. Functional structure of the organ of corti - a review. Hear. Res. 22 (1–3), 117–146. https://doi.org/10.1016/0378-5955(86)90089-4.

Liu, S., White, R.D., 2008. Orthotropic material properties of the gerbil basilar membrane. J. Acoust. Soc. Am. 123 (4), 2160–2171. https://doi.org/10.1121/1.2871682.

Muller, M., 1996. The cochlear place-frequency map of the adult and developing Mongolian gerbil. Hear. Res. 94 (1–2), 148–156. https://doi.org/10.1016/0378-5955(95)00230-8.

Murakoshi, M., Suzuki, S., Wada, H., 2015. All three rows of outer hair cells are required for cochlear amplification. BioMed Res. Int. 12, 727434 https://doi.org/10.1155/2015/727434, 2015.

Nam, J.-H., 2014. Microstructures in the organ of corti help outer hair cells form traveling waves along the cochlear coil. Biophys. J. 106 (11), 2426–2433. https://doi.org/10.1016/j.bpj.2014.04.018.

Nam, J.-H., Fettiplace, R., 2010. Force transmission in the organ of corti micromachine. Biophys. J. 98 (12), 2813–2821. https://doi.org/10.1016/j.bpj.2010.03.052.

Ni, G., Elliott J., S., 2013. Effect of basilar membrane radial velocity profile on fluid coupling in the cochlea. J. Acoust. Soc. Am. 133 https://doi.org/10.1121/1.4789863.

Ni, G., Elliott, S.J., Baumgart, J., 2016. Finite-element model of the active organ of Corti. J. R. Soc. Interface 13 (115), 20150913. https://doi.org/10.1098/rsif.2015.0913.

Ni, G.J., Sun, L.Y., Elliott, S.J., 2017. A linearly tapered box model of the cochlea. J. Acoust. Soc. Am. 141 (3), 1793–1803. https://doi.org/10.1121/1.4977750.

Nuttall, A.L., Guo, M.H., Ren, T.Y., 1999. The radial pattern of basilar membrane motion evoked by electric stimulation of the cochlea. Hear. Res. 131 (1–2), 39–46. https://doi.org/10.1016/s0378-5955(99)00009-x.

Raphael, Y., Altschuler, R.A., 2003. Structure and innervation of the cochlea. Brain Res. Bull. 60 (5–6), 397–422. https://doi.org/10.1016/s0361-9230(03)00047-9.

Raphael, Y., Lenoir, M., Wroblewski, R., Pujol, R., 1991. The sensory epithelium and its innervation in the mole rat cochlea. J. Comp. Neurol. 314 (2), 367–382. https://doi.org/10.1002/cne.903140211.

Ren, T.Y., He, W.X., Kemp, D., 2016. Reticular lamina and basilar membrane vibrations in living mouse cochleae. Proc. Natl. Acad. Sci. U.S.A. 113 (35), 9910–9915. https://doi.org/10.1073/pnas.1607428113.

Robles, L., Ruggero, M.A., 2001. Mechanics of the mammalian cochlea. Physiol. Rev. 81 (3), 1305–1352.

Soons, J.A.M., Ricci, A.J., Steele, C.R., Puria, S., 2015. Cytoarchitecture of the mouse organ of corti from base to apex, determined using in situ two-photon imaging. JARO J. Assoc. Res. Otolaryngol. 16 (1), 47–66. https://doi.org/10.1007/s10162-014-0497-1.

Steele, C.R., Baker, G., Tolomeo, J., Zetes, D., 1993. Electro-mechanical Models of the Outer Hair Cell.

Steele, C.R., Lim, K.M., 1999. Cochlear model with three-dimensional fluid, inner sulcus and feed-forward mechanism. Audiol. Neuro. Otol. 4 (3–4), 197–203. https://doi.org/10.1159/000013841.

Steele, C.R., Puria, S., 2005. Force on inner hair cell cilia. Int. J. Solid Struct. 42 (21–22), 5887–5904. https://doi.org/10.1016/j.ijsolstr.2005.03.056.

von Bekesy, G., 1970. Travelling waves as frequency analysers in the cochlea. Nature 225 (5239), 1207–1209. https://doi.org/10.1038/2251207a0.

Yoon, Y.J., Steele, C.R., Puria, S., 2011. Feed-Forward and feed-backward amplification model from cochlear cytoarchitecture: an interspecies comparison. Biophys. J. 100 (1), 1–10. https://doi.org/10.1016/j.bpj.2010.11.039.

Zagadou, B.F., Barbone, P.E., Mountain, D.C., 2020. Significance of the microfluidic flow inside the organ of corti, 12 J. Biomech. Eng. Trans. ASME 142 (8), 081009. https://doi.org/10.1115/1.4046637.

Zetes, D.E., Tolomeo, J.A., Holley, M.C., 2012. Structure and mechanics of supporting cells in the Guinea pig organ of corti. PLoS One 7 (11), e49338. https://doi.org/10.1371/journal.pone.0049338.

Zwislocki, J.J., Cefaratti, L.K., 1989. Tectorial membrane II: stiffness measurements in vivo. Hear. Res. 42 (2), 211–227. https://doi.org/10.1016/0378-5955(89)90146-9.